3-Dimensional dynamics of the galactic bulge

Soto Vicencio, M.H.

Citation

Soto Vicencio, M. H. (2010, March 24). *3-Dimensional dynamics of the galactic bulge*. Retrieved from https://hdl.handle.net/1887/15120

CHAPTER 2

Radial Velocities for 6 bulge fields: Procedures and results

M. Soto, R.M. Rich, K. Kuijken

to be submitted

The detailed structure of the galactic bulge still remains uncertain. The strong difficulties of obtaining observations of stars in the galactic bulge have hindered the acquisition of a kinematic representation for the inner kpc of the Milky Way. The observation of the 3-d kinematics in several low foreground extinction windows can solve this problem. We have developed a new technique, which combines precise stellar HST positions and proper motions with integral field spectroscopy, in order to obtain reliable 3-d stellar kinematics in crowded fields of the galactic center. In addition, we present results using the new techniques for six fields in our project. A significant vertex deviation has been found in some of the fields in agreement with previous determinations. This result confirms the presence of a stellar bar in the galactic bulge.

2.1 INTRODUCTION

The Milky Way bulge is the nearest example of a bulge/spheroidal population that we can observe. Its closeness allows us to resolve stellar populations and the associated kinematics, something which is not possible in external galaxies. Even though many data have been gathered, a detailed unified picture of the galactic bulge including abundances, stellar populations and kinematics is far from being completed.

One of the main difficulties is the location of the Sun inside the disk dust layer, which limits observations to a few windows where the foreground dust extinction is relatively low. In addition, populations in these windows are projected on top of each other, complicating the analysis. Disk and bulge components overlap in the color-magnitude diagram specially near the turn-off (Holtzman et al. 1998), hampering a selection based on photometric criteria alone.

In spite of these limitations, important information has been gathered over the years. One of the pioneering studies of the kinematics of the galactic bulge was that of Spaenhauer et al. (1992), who measured proper motions for ∼400 stars from photographic plates obtained in 1950 and 1983. This proper motion sample was the basis for subsequent abundance and radial velocity studies of the original proper motion sample (Terndrup et al. 1995, Sadler et al. 1996). Zhao et al. (1994) combined the results of these studies with those obtained previously by Rich (1988, 1990), and compiled a small subsample of 62 K Giants with 3-d kinematics and abundances. In spite of its small size the subsample showed a significant vertex deviation, a signature of barlike kinematics. This result has recently been confirmed with a larger sample of ∼300 stars (this thesis, chapter 3). de Vaucouleurs (1964) had originally suggested that our galactic bulge was actually barred, based on the similarity of its spiral structure with other galaxies with strong bars. Nevertheless, direct stellar signatures of the barlike structure had not been found before.

In addition to models of the stellar distribution (e.g. Zhao et al. 1996a) gas observations and hydrodynamical models also have been used to study the galactic bulge (e.g. Englmaier & Gerhard 1999). Many of these models rely on three dimensional deprojections of the galactic bulge derived from the COBE DIRBE images (Dwek et al. 1995) whose results showed asymmetries consistent with a stellar bar in the galactic center. Even though all analyses agree on the rough orientation of the bar, complete agreement about the values of the parameters which would define this bar, such as rotational bar pattern speed or position angle has not been reached yet. For example, values for the angle between the bar's major axis and our line of sight to the galactic center have ranged from $\sim 20^\circ$ in the first galactic quadrant (e.g. Binney et al. 1991) to 44° in a recent new determination by Benjamin et al. (2005) using Spitzer infrared star counts.

Understanding the bulge kinematics requires understanding the gravitational potential that drives the orbits (Kuijken 2004, henceforth K04). Once the kinematics are understood, they can be correlated with stellar population information to build a picture of the galaxy evolution and bulge formation scenario.

In order to improve our knowledge of the stellar kinematics in the bulge region we have embarked on a project to obtain three-dimensional velocities for a large sample of bulge stars, by combining HST proper motions measurements with VIMOS spectroscopy.

In this paper we present integral-field (IFU) spectroscopic measurements for six bulge fields that have HST proper motion measurements: three fields on the minor axis (Kuijken & Rich 2002, henceforth KR02; KR04) as well as three fields at positive longitudes. We have combined the IFU data cubes with photometric information in a new procedure designed to work in crowded fields; the technique combines the precise HST photometry and IFU spectroscopy to optimize the spectral extraction.

Stellar kinematics involves the measuring the phase-space distribution function. This phase space generally has three degrees of freedom. By providing 4-6 coordinates per star (the two proper motions, two sky coordinates, a distance determination by means of a main sequence photometric parallax, and a radial velocity for a subsample of bright stars) we will overconstrain the phase-space distribution in order to allow us a reliable determination of the orbit structure.

The outline of this paper is as follows. In section 2 we will briefly explain the project of which the work presented in this paper is a part, section 3 is an account of the observations and the methods involved in each case. Section 4 contains the results of our analysis. Finally section 5 is the summary and conclusions for this work.

2.2 PROJECT

The HST data archive contains a treasure in WFPC2 images taken during the nineties. This wealth of images can be used to find suitable first epoch fields for proper motion work; we have chosen ten for this project, our criteria: low foreground extinction, good exposures, and spread in l and b. Hence, the HST archive has provided us with first epoch observations in six fields at $l \sim 0$, and $l > 0$; in addition, we have established four fields at $l < 0$ in order to target both ends/sides of the bar/bulge. The goals for each field are the acquisition of color magnitude diagrams, accurate astrometry, and radial velocities for as many stars as possible.

Figure 2.1 shows all the fields for this project. HST archive images were primarily used to set first epoch proper motion exposures in several low extinction bulge regions, close to the galactic minor axis and at positive longitudes. These initial fields were complemented more recently with observations in four more fields at negative longitudes. Thus, this project strategically spans a wide range of bulge locations, sampling a significant stellar population at the center and both sides of the bulge/bar. Consequently, the proper motion results published in KR02 and K04, represent the first important piece of kinematic information on this project, which we continue here. The complete HST programme described before, which points to proper motions, photometry and parallax distances has been more recently combined with a spectroscopic VLT programme in the same fields, this spectroscopic information, and the techniques involved are the subject of this paper, where Table 2.1 shows the coordinates of each field.

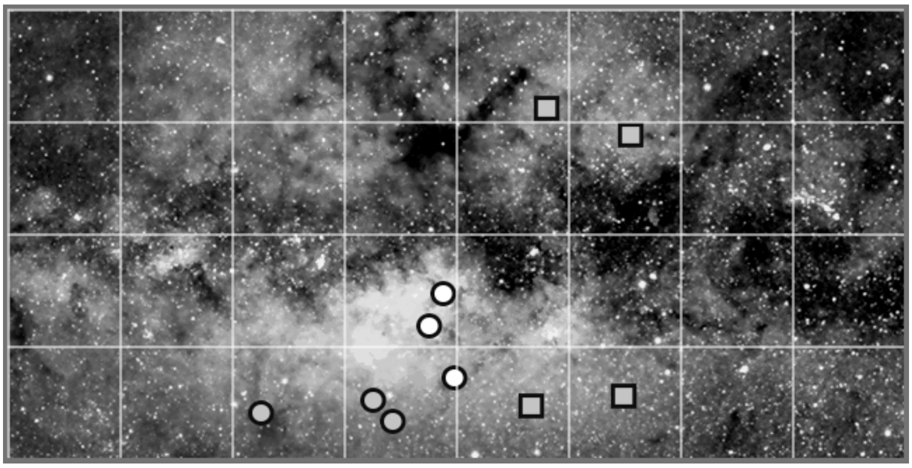

Figure 2.1: Fields in the Galactic Bulge observed for this project, superimposed on an optical map, from longitude +20° to -20°, and latitude -10° to +10°. White and grey circles correspond to fields for which proper motion and radial velocity measurements have been completed. Data sets for the four fields at negative longitudes (grey squares) have not been completed so far.

2.3 OBSERVATIONS AND PROCEDURES

2.3.1 Proper motions

First epoch photometric observations with WFPC2 for all the fields used in this paper were obtained from the Hubble Space Telescope data archive. In the case of the three fields close to the galactic minor axis (near l =0°) second epoch observations over a time baseline of 6 years have resulted in accuracies better than 1 mas/yr, which corresponds to errors below 30 km/sec at the distance of the bulge, significantly smaller than the velocity dispersion of the bulge of 100 km/sec. Even longer time baselines for the fields at positive longitudes were used (8-9 years) as Table 2.1 shows. First and second epochs were taken with WFPC2 for fields close to the galactic minor axis, conversely fields at positive longitudes used a combination of WFPC2 and ACS for first and second epoch respectively. The latter fields thus had to include small differences in the procedure to take into account the instrument change (e.g. the shearing of ACS images with respect to WFPC2).

Table 2.1 shows epochs and positions of the proper motion data with WFPC2 and ACS. Proper motions were measured using a modification of the Anderson & King (2000) procedure, which consists of a combination of PSF reconstruction and PSF core fitting (KR02). A more detailed account about the proper motion measurements can be found in KR02 and it will not be repeated here.

2.3.2 Radial Velocities

The procedure to obtain the spectrum of each star in these crowded fields consists of two main steps, the extraction of the spectra for each fiber/pixel in the IFU field, and

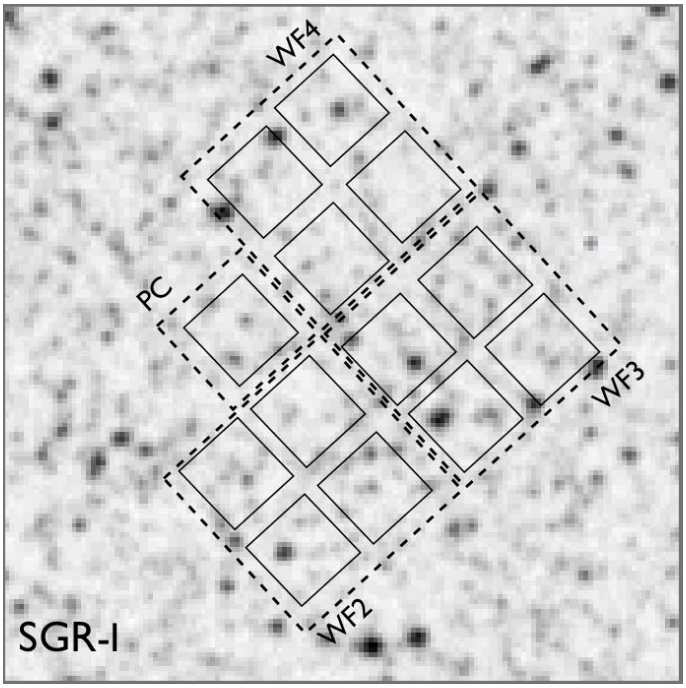

Figure 2.2: Finding chart for one of our fields, *Sagittarius-I*, using an image from 2MASS. Each small square (solid line) corresponds to each one of the VIMOS IFU fields. Dashed squares correspond to PC, WF2, WF3 and WF4 HST fields superimposed on the same image.

the extraction of the star spectra from the IFU data cube. During the second step we will combine the spectroscopy with the information yielded by HST imaging.

The VLT VIMOS Integral Field Unit (IFU) has a 27″×27″ field of view in high resolution (R ∼2050) which allows spectra to be taken on a 40 × 40 grid simultaneously. Thus, this instrument allows to target a high number of bulge stars in every exposure with a high spectral accuracy (a spectral dispersion of 0.56 Å/pixel), where the blue

Table 2.1: Radial Velocity and Proper-Motion Fields.

Field	PM Epoch	PM Instrument	(l,b)	α, δ (J2000.0)
Baade's Window	1994 Aug	WFPC2	(1.13, -3.76)	18 03 10, -29 51 45
	1995 Sep	WFPC2		
	2000 Aug	WFPC2		
Sgr-I	1994 Aug	WFPC2	(1.26, -2.65)	17 59 00, -29 12 14
	2000 Aug	WFPC2		
NGC 6558	1997 Sep	WFPC2	(0.28, -6.17)	18 10 18, -31 45 49
	2002 Aug	WFPC2		
Field 4-7	1995 Jul	WFPC2	(3.58, -7.17)	18 22 16, -29 19 22
	2004 Jul	ACS/WFC		
Field 3-8	1996 May	WFPC2	(2.91, -7.96)	18 24 09, -30 16 12
	2004 Jul	ACS/WFC		
Field 10-8	1995 Sep	WFPC2	(9.86, -7.60)	18 36 35, -23 57 01
	2004 Jul	ACS/WFC		

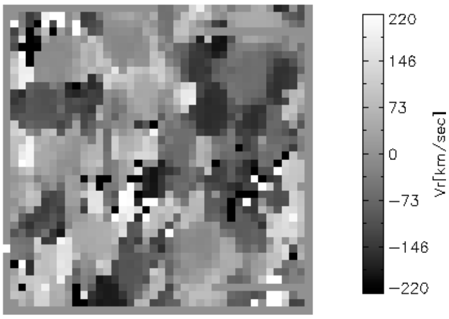

Figure 2.3: Velocity field for one of our IFU observations in Baade' window. The velocity for each pixel/fiber has been calculated using cross-correlation, where each fiber corresponds to 0.66" . The VIMOS-IFU instrument allows clearly to distinguish between adjacent stars with different kinematics.

Table 2.2: Summary of Radial Velocity Observations .

Field	1^{st} run (2003)	2^{nd} run (2006)	3^{rd} run (2007)	Total IFU Fields	Stars with Rad. Vel.
Baade's Window	5	5	4	14	965
Sgr-I	5	6	5	16	962
NGC 6558	5	5	4	14	766
Field 4-7	0	8	3	12	664
Field 3-8	0	10	3	13	466
Field 10-8	0	9	4	13	756

filter used has a wavelength range spanning from 4150 to 6200 Å. We used this instrument to target our HST fields, which can each be covered by 13 VIMOS pointings (4 per WF chip and 1 per PC, as Figure 2.2 illustrates for Sagittarius-I). Each IFU pointing was exposed for 2 × 1000 sec , which has allowed us to resolve approximately 80 stars per IFU field. The spectra yield 30 $km\ s^{-1}$ radial velocity precision, which is well-matched to the transverse velocity accuracy from our proper motions (better than 1 mas/yr, equivalent to ~30 $km\ s^{-1}$ at 8 kpc distance), and sufficient to resolve the velocity dispersion in the central parts of the Galaxy, which is about 100 $km\ s^{-1}$.

In addition to the regular science images containing the information about our six HST fields, we included regular observations of dark bulge regions to substract them from the science images as sky, we will refer to this later in this section. Standard stars were observed as well, for use as templates in the cross-correlation process for the determination of the velocities. The overall observation time for all the spectral observations was 17, 50 and 45 hours for our three observing runs respectively. Table 2.2 summarizes the VIMOS IFU observations for the six fields presented in this paper. In Table 2.2 the numbers under every "run" column correspond to the number of IFU fields observed in that run. All data was taken in service mode with seeing conditions constrained at a maximum of 0.8".

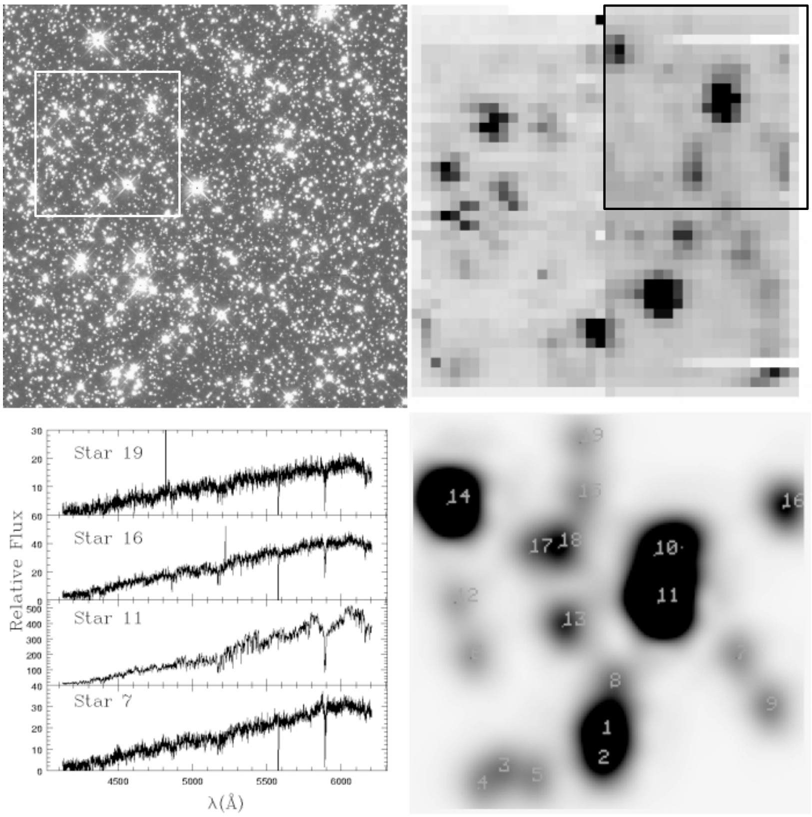

Figure 2.4: Steps during the process to build a star spectrum from the spectral cube. The top left figure corresponds to one of our observations with HST WF2 in Baade's window, the white square corresponds to the area covered by one of the VIMOS IFU images (top right). In the IFU field the first quadrant is enclosed, its respective convolved image produced during the deconvolution process to check the detection of stars in the first quadrant appear at the bottom right. Finally some examples of the spectra extracted by this process are shown at the bottom left.

Data cube organization and Radial velocity measurements

VIMOS IFU raw data are complex to reduce and calibrate. Fiber spectra extraction was carried out using the ESO pipeline for VIMOS IFU data. Programs GASGANO[1] and

---

[1] available at http://www.eso.org/observing/gasgano/

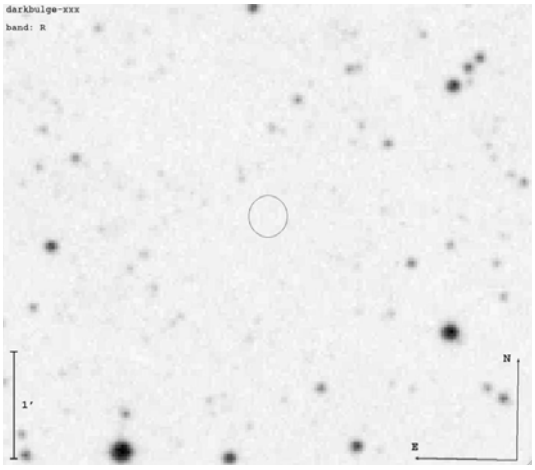

Figure 2.5: Finding chart of one of our darkbulge fields (circle in the middle) over a 2MASS image. Darkbulge fields have been used during the sky subtraction in VIMOS IFU fields.

ESOREX[2] were used to manage the VIMOS IFU recipes[3] (Details about methods and procedures of the recipes can be found in VIMOS pipeline User's Guide and Gasgano User's Manual). The recipes used during our processing were *vmifucalib* and *vmifuscience*.

The final product of the VIMOS IFU recipes are the spectra extracted and wavelength calibrated in one image that includes all the spectra for each quadrant in the IFU field.

An important problem to be considered in spectroscopic reduction is related to the sky subtraction, which has not been implemented by the VIMOS pipeline (VIMOS Pipeline User's Guide 7.23.11). We have tried two approaches. The first is basically the same recommended by the VIMOS Pipeline User's Guide. We took the 20 spectra with lowest signal per quadrant (which means 5% of the total) and averaged them (taking care to reject dead fibers). The combined spectrum was considered as sky and subtracted from the rest of the fibers. This way of proceeding is extremely risky and could change the results that we seek by subtracting a flux level too high (or too low) from the reduced spectra. The second method involves exposures of nearby highly extincted 'dark bulge' fields, whose spectra, appropriately scaled mimic the sky contribution to the stellar fields as Figure 2.5 shows.

Both processes were extensively tested to check their influence on our radial velocity results; we found no significant differences for both procedures, typically below 3 $km\ s^{-1}$ in the final velocity measurements per fiber. Given the reliability of our extraction we have preferred to use the sky extraction by dark fields in our fields.

Once the spectra were reduced we assembled them into spectral data cubes. In addition to the regular calibrations, we produced for each IFU field, a response map to check the normal behavior of the fibers through the field. Dead fibers or lost traces are easily highlighted in this way.

The last step is the radial velocity measurement per fiber in each IFU field. The measurement of radial velocities was made in all cases using a cross correlation us-

---

[2] available at http://www.eso.org/observing/cpl/download.html

[3] available at http://www.eso.org/observing/gasgano/vimos-pipe-recipes.html

ing the IRAF task *fxcor* (Tonry & Davis 1979) with a template standard star. Before the cross correlation some zones of the spectra were masked; for instance the atmospheric emission line due to OI at 5577.5 Å; or the interstellar absorption NaD lines at 5889 Å. The latter lines are particularly strong in K2-3 III Giants, and can easily bias the correlation with our template to calculate velocities or a possible spectral type classification. An example of the velocity field calculated with the procedure here described for one of our IFU fields in Baade's window appears in Figure 2.3, and clearly shows distinct colored zones which correspond to different stars at different velocities. Extracting this information optimally is the subject of the next section.

Deconvolution

As shown in Figure 2.4, the bulge fields are very crowded, and therefore, a reliable technique to correct IFU spectra cubes for blending is absolutely necessary. Fortunately, our HST images allow us to know precisely where the stars are. This information makes feasible the optimal extraction of star spectra from the IFU cubes.

The first step to carry out the deconvolution process is a coordinate transformation from HST to IFU coordinates, which is performed using the standard IRAF tasks *daofind* and *geomap*. Since not all the stars observed in the HST image are detected in the IFU field, a threshold magnitude for the HST list stars must be given. In the case of the fields SgrI, and BW, for which we have F555W observations, this limiting magnitude was set at $V(F555W)_{lim}$=21 mag. Similarly, for fields NEAR NGC6558 (which is actually located close to NGC 6558), Field 4-7, Field 3-8, and Field 10-8 the limiting magnitude is $V(F606W)_{lim}$=20-20.5 mag, depending of the particular crowding in the IFU field. Using this limiting magnitude we avoid the deconvolution of the complete list of stars detected in the HST image, where naturally a large fraction of them are beyond the detection limit of the VIMOS IFU observations.

Armed with a magnitude-limited list of HST proper motions, positions, and magnitudes, we have produced a procedure which accounts for defects in the HST list to separate the fluxes of as many stars as possible from the VIMOS IFU spectral cube. Thus, the HST list, once cleaned from spurious stars due to failures in the DAOFIND detection procedure at 20 σ, is used to perform the deconvolution of the stellar spectra in the IFU cube. The deconvolution requires a precise IFU PSF and the HST positions in the IFU field . Simultaneously, a convolved image using the HST magnitudes and positions and the IFU PSF is created during the deconvolution process. This convolved image yields an estimation of blending for each star which is used to select stars with a limited amount of blending for the final list of stars with radial velocities after the deconvolution. Hence, once stars have been deconvolved from the IFU-cube from a HST cleaned list, we can measure our radial velocities.

This deconvolution procedure can be described in more detail as follows: With the final list of cleaned HST stars lying in the respective IFU field and the PSF of the latter we can estimate the contribution of a star s to each pixel i, which defines the model,

$$P_i = \sum_s F_s C_{si}, \tag{2.1}$$

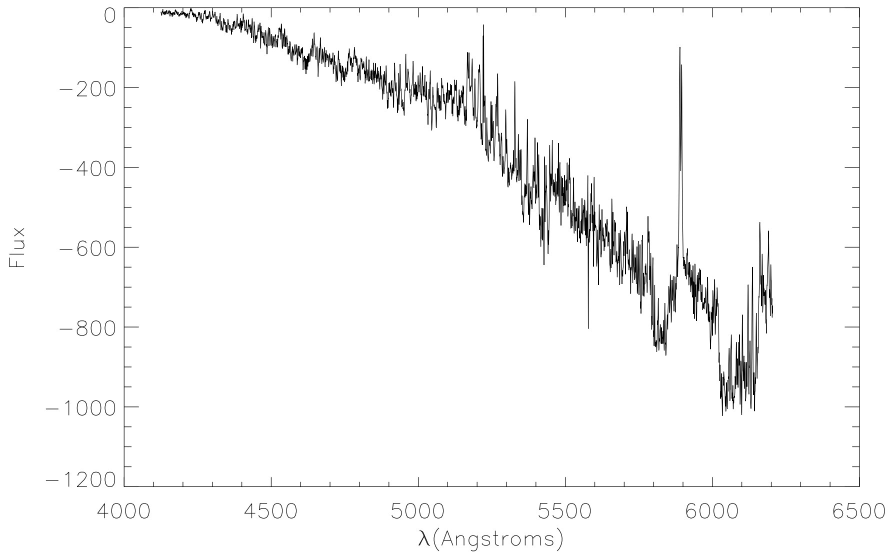

Figure 2.6: Example of the result of using a wrong PSF during the deconvolution. This is the deconvolved spectrum for the HST position in the star 11 in Figure 2.4 obtained using a modified PSF. The flux overestimation in a neighbor star by the PSF produces, when the system is solved, a negative solution for this star. A correlation can not be established with these distorted spectra in the radial velocity measurements.

where P_i is the flux in each pixel, F_s is the flux in the star s and C_{si} corresponds to the contribution of that star s to the pixel i obtained using the IFU PSF.

$$\chi^2 = \sum_i (P_i(observed) - P_i(model))^2 \tag{2.2}$$

$$= \sum_i (P_i(observed) - \sum_s F_s C_{si})^2, \tag{2.3}$$

which can be solved by requiring

$$\frac{\partial \chi^2}{\partial F_s} = 0 \qquad \forall s. \tag{2.4}$$

This results in the matrix showed in eq. 2.5

$$\sum_{s'} F_{s'} \left(\sum_i C_{si} C_{s'i} \right) = \sum_i P_i C_{si}, \tag{2.5}$$

which defines a square system. The solution of this matrix for each slice of the IFU data corresponds to the flux solution to that wavelength for each star; repeating the procedure in every slice of the cube we are able to reconstruct the spectrum of each star.

This technique, simple in theory, might yield a singular matrix in some cases, when stars are too close of each other in the HST image, and therefore can not be resolved in the IFU image. Furthermore, saturation and bleeding would augment the probability of obtaining a singular matrix in eq. 2.5, as these effects produce multiple DAOFIND detections around saturated spots. In order to avoid a singular matrix during the deconvolution procedure, we have implemented several solutions, which we describe below: (1) Due to the differences in the pixel scale and resolution between the HST WFPC2 and the VIMOS IFU image (pixel scale is 0.05″ for PC,and 0.1″ for WF, while each pixel/fiber is 0.66″ in VIMOS-IFU) it is expected that in many cases more than one HST star will fall in one single IFU pixel. Even in those cases, the fluxes of two stars in the same IFU pixel can be separated as long as they can be resolved as single stars using the IFU PSF and the HST positions. The IFU PSF has a typical FWHM in our observations of 1.8 pixels. Thus, we have found realistic to set a minimum blending radius for the stars in the HST list, stars closer than 0.01 IFU pixel-scale have been considered as one during the deconvolution, where fluxes have been added in those cases. (2) Similarly, false detections due to bleeding and saturation in the HST list are discarted by comparing with the positions of stars in the IFU field, crossing both lists, we identify the HST star position which is closer to the position detected in the IFU field, discarding the rest of the detections in the HST list inside an avoidance radius. Typically an avoidance radius of 0.5×FWHM of the IFU PSF has been used. (3) Nevertheless, in spite of the two procedures just described, false DAOFIND detections in the HST list have eventually appeared during the deconvolution. These false stars in the HST list were particularly common in long exposures, where saturation and bleeding in bright stars left saturation many pixels away of the central position of the star. In order to solve this we have devised a simple local procedure which iteratively compares the convolved image generated by the HST position, magnitudes, and the IFU PSF with the real IFU field image; stars in the HST list with fluxes $2 \times background$ of a ratio image (real IFU image divided by a simulated IFU convolved image) are rejected and marked as false stars to generate a new convolved image and a new loop. This iterative process rapidly converges and effectively cleans of false stars due to saturated pixels the HST list of stars. (4)Finally, once the deconvolution is performed, a final selection is carried out, as we mentioned before. This last selection is intended to avoid stars which are blended, mixing different populations, which due to our radial velocity measurement technique, would deliver an average velocity as a result. Hence, we measure as many velocities as possible in single stars. Only stars in which the central positions had at least 70 % of the total flux of the pixel were finally selected. An example of this process and its results is illustrated in Figure 2.4.

A limitation of our technique is related to the PSF construction. The IFU field is small as we have already mentioned, which combined with the area covered for each fiber (0.66″), allows only a few detections in each IFU exposure (∼40-80 typically, in normal conditions, with the four quadrants working). This small number of detections often produces a heavily undersampled PSF , which is critical in the deconvolution, where this PSF is used as a model to estimate the flux of every star.

During the development of our procedure each PSF was carefully obtained. The result of using a wrong PSF produces a flux overestimation of some stars. The result of this overestimation is negative fluxes in stars in the neighborhood of some bright stars

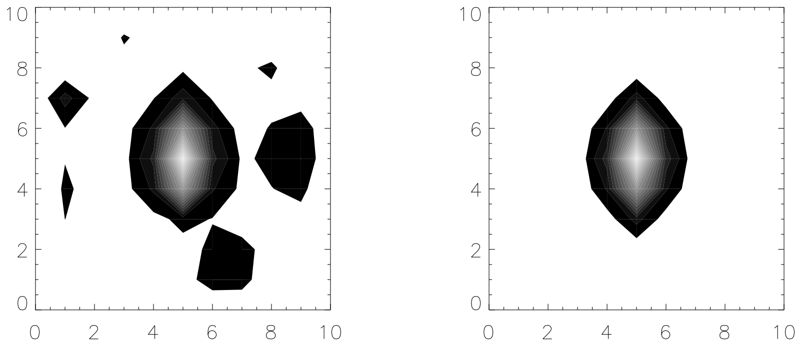

Figure 2.7: Example of procedure to "refit" a IFU PSF. The undersampling of the IFU PSF is fixed by a new fitting procedure which gives more weight to central pixels in order to avoid background noise and contamination by neighbor stars. The new PSF is used during the deconvolution process.

which, when projected to all the wavelengths in the spectral cube corresponds exactly to the spectrum of the neighbor bright star inverted as it is shown in Figure 2.6. A similar result is obtained when many HST positions are located in the proximity of a very bright star, which is a typical failure of photometric detection in bright saturated stars. In all these cases it is not possible to obtain a reliable radial velocity measurement for these inverted spectra. Limited solutions implemented in our code, and already described, relate and compare the stars detected in the HST and VIMOS IFU field in order to solve the crowding. The undersampling of the IFU PSF on the other hand requires additional information. In order to improve this undersampled IFU PSF we performed, a Gaussian *"refitting"* of the IFU PSF generated by IRAF tasks, where several PSF models were tested. The PSF fit gives more weight to central pixels, where differences in background flux between original and refitted PSF were typically of the order of 3% and did not show significant consequences in the final velocity results. An example of the latter procedure is shown in Figure 2.7, and a summary of all radial velocity measurements for our the six fields is indicated in table 2.2.

An alternative deconvolution

Since deconvolution and cross-correlation are both linear operators, they can be carried out in any order. Thus, an equivalent procedure to deconvolve the cross-correlation function (CCF) obtained from the velocity measurements of all fibers in the quadrant has been implemented. The procedure separates the contributions of the flux of each star in each pixel in the CCF data cube in the same way that spectra for all the stars are deconvolved from the spectra data cube. Consistency between the velocity results using both methods has been proven. Figure 2.8 shows the CCF from the same star in both cases; the maximum in the deconvolved CCF is found at the same pixel position, where each pixel corresponds to 31.78 km/sec. Thus, the deconvolution needs to be run on just a few pixels around the velocity zero channel. At high spectral resolution

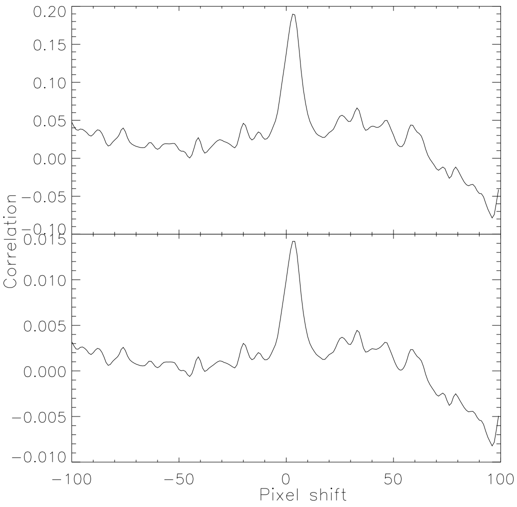

Figure 2.8: Cross-correlation function for one of the stars in Baade's Window field. (*Top*) Obtained from the velocity measurement of the deconvolved spectrum. (*Bottom*) Obtained directly from the deconvolution of the CCF data cube

the CCF deconvolution could be an interesting way to deblend data cubes spectrally.

Saturation not only affected our deconvoltution procedure by adding false stars in the HST DAOFIND, also it affected the estimation of the amount of blending, and therefore the final selection of stars in the IFU spectral cube. The problem of saturation affecting the values of the magnitudes, was specially significant in NEAR NGC 6558 and the three off-axis fields, which count with first epoch HST observations originally intended for the study of faint stars, and therefore with long exposure times. The latter problem was partially solved with the calculation of *m814* aperture photometry magnitudes from short exposures (50 sec.) of the ACS second epoch images. This was possible only for the three off-axis fields Field 4-7, Field 3-8, and Field 10-8. Consistency of the velocity results has been checked using both magnitudes, showing no differences and therefore allowing us to avoid many misidentification, after the deconvolution in these fields.

2.3.3 Zeropoint Velocity Corrections

Our data combine three observing runs as Table 2.2 shows. In order to check the reliability and performance of our technique we repeated in each observing run one of our fields in Sagittarius-I. *Sgr1-pc* has a reasonable crowding, with a lack of very bright stars, and represents a typical example of the performance of VIMOS IFU during our bulge observations.

Each year's observations were analyzed with the same HST master list, and reduced independently. Figure 2.9 shows a comparison of the radial velocities obtained. A small but significant offset is evident between the observing seasons. Even though the origin of these deviations has not been identified completely, we have corrected

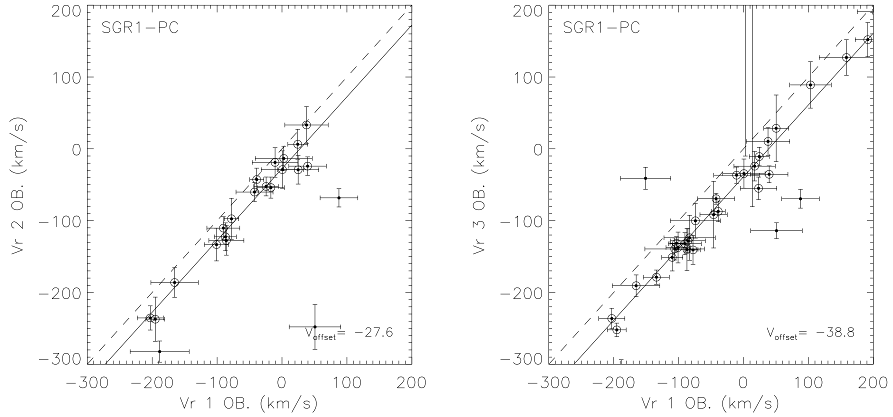

Figure 2.9: Velocity zeropoint determination for second and third run IFU fields. IFU field *Sgr1-pc* velocity results have been compared between the first and second observing run (*left*), and first and third (*right*). The fit in each case is iterative, rejecting stars beyond 40 km s^{-1} of a slope 1 linear fit. Those stars selected in the final iteration are enclosed by a circle.

them in each case. Thus, a zeropoint offset has been added to the observations of the second and third observing runs, of 27.6 and 38.8 (km s^{-1}) respectively. One possible explanation to this problem could be related to our standard star HD157457, which corresponds to a star in a double system, and therefore susceptible to velocity changes over periods comparable to the time elapsed between our observing runs. Consequently, standard star observations have been cross correlated, comparing their measured velocities with respect to the first run. The latter test delivered similar differences to those found fitting the zeropoint of measurements in *Sgr1-pc*. It has been also checked that this zeropoint is not an artifact particularly related to one of the observations in *Sgr1-pc*. An additional field in Sagittarius-I, *Sgr1-WF2d* which was partially repeated in the third run concords with the offset first found in *Sgr1-pc*.

2.4 ANALYSIS

2.4.1 Velocity results in fields close to the galactic minor axis and off-axis fields

Table 2.3 and Figure 2.10 show our velocity results. We only selected ~ 3200 radial velocities for these plots, which correspond to stars with velocity errors $\leq 50\ km\ s^{-1}$. Gaussian fits have been calculated for each velocity distribution, where FIELD 10-8 required a bimodal fit since it corresponds to the sum of the distribution of NGC 6656 (also known as M22) and (presumably) bulge stars in the field.

Our three minor axis fields Sagittarius-I, Baade's Window and NEAR NGC 6558, which target denser parts of the bulge, account for the majority of the results (~2000 radial velocities), while the rest (~1000 radial velocities) are more or less equally distributed between the off-axis fields FIELD 4-7, FIELD 3-8, and FIELD 10-8. Sagittarius-I

Table 2.3: Radial Velocity Distribution and Gaussian fit parameters.

Field	N_{stars}	Centre (km s^{-1})	σ (km s^{-1})	Kurt
Baade's Window	781	2	130	0.065
Sgr-I	773	1	123	0.009
NGC 6558	563	-11	72	2.328
FIELD 4-7	488	11	84	2.132
FIELD 3-8	289	-12	60	4.295
FIELD 10-8 [a]	193(381)	-34	96	1.324
FIELD 10-8 [b]	231(381)	-149	17	5.203

[a] Distribution of field stars

[b] Distribution from NGC 6656 stars in FIELD 10-8.

and Baade's Window have high velocity dispersions, which agree well with previous determinations in BW (Soto et al. 2007, McWilliam & Rich 1994, Sadler et al. 1996) and the galactic rotation and velocity dispersion curves based on K-giants and M-giants (Minniti 1996, and Rich et al. 2007, respectively) at several longitudes (Figure 2.11). However, there are clear differences between these two distributions, BW clearly does not resemble a Gaussian as accurately as Sagittarius-I. Thus, in spite of its closeness, both fields seem to represent slightly different kinematic populations inside the galactic bulge. On the other hand, NEAR NGC 6558 shows a small dispersion compared with the other two minor-axis fields, and it is under the curve of velocity dispersion of the galaxy. Conversely, NEAR NGC 6558 agrees with the bulge rotation curve. In addition, the three minor axis fields show a clear dispersion gradient in galactic latitude. Consistently, kinematic differences between these fields were also seen in proper motions (K04).

In our off-axis fields we found that Field 4-7 and Field 3-8 seem to show a reasonable agreement with the bulge rotation curve. Conversely, FIELD 10-8 does not show a good agreement. This apparent disagreement in the latter field might be caused by strong contamination by non-bulge stars (mainly cluster), or by poor statistics. Therefore, in order to avoid some of the possible contamination by cluster stars in Field 10-8, , we have used for the galactic rotation curve the respective Gaussian fit value. This Gaussian fit value for the dispersion agrees well with the galactic rotation curve. Other authors have previously explored contamination rates in Field 10-8. (Minniti et al. 1996)

A key aim of our work is to derive space motions for a large sample of bulge stars, combining radial radial velocities and proper motions. As shown in KR02 main-sequence stars below the turn-off show a proper motion drift consistent with a foreground disk population rotating in front of the bulge, whereas red giants show kinematics representative of the bulge population as a whole. We attempt to remove foreground stars via cuts in the CMD as it is shown in Figure 2.12.

Unfortunately, no such cuts could be applied to the NEAR NGC 6558 field, for

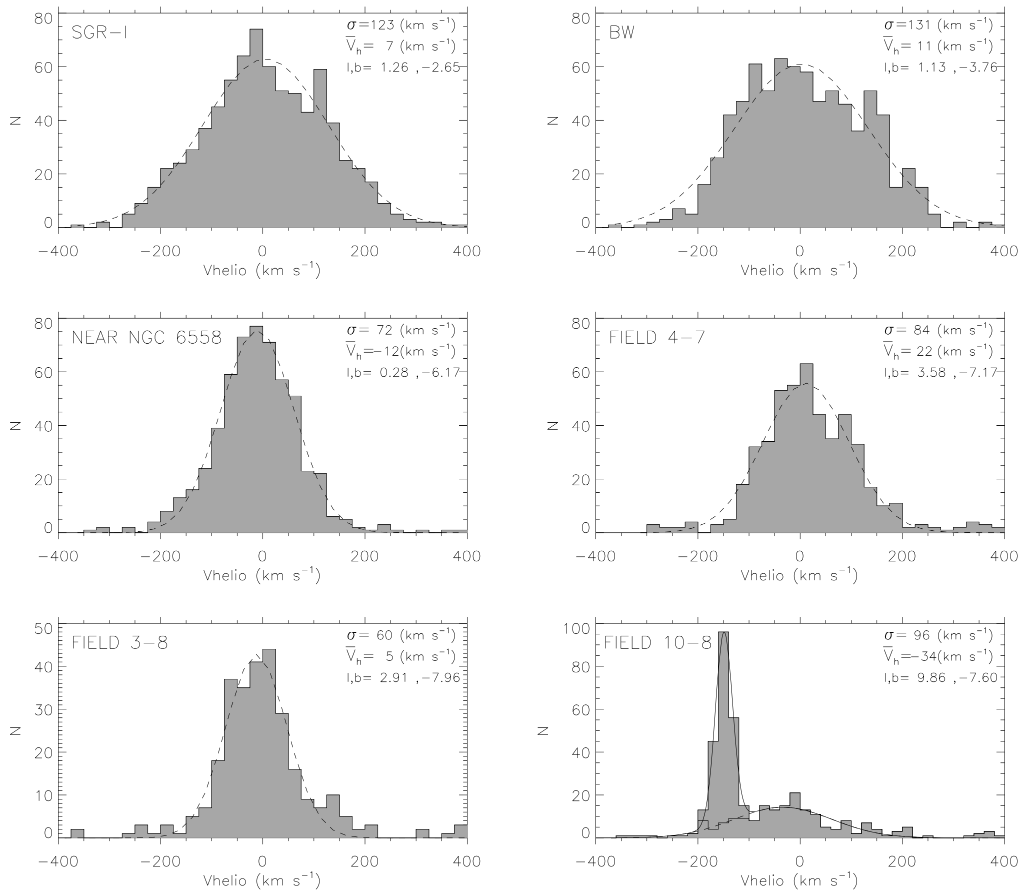

Figure 2.10: Velocity histograms for our six fields. A Gaussian fit has been performed in all the cases.

which no suitable archival first epoch images are available, giant and turn-off stars appear saturated on the respective CMD. Hence proper motions are only available for fainter stars in this field. We expect disk contamination to be a minor problem at the latitude of this field. Our three minor-axis fields, whose results we analyze here, SGR-I, Baade's window and NEAR NGC 6558 lie close to the galactic minor axis. An axisymmetric bulge should produce at those longitudes velocity ellipsoids aligned with the line of sight. Therefore, any deviation of that alignment in the velocity ellipsoid or vertex deviation is a clear signature of a non-axisymmetric bulge.

Specifically, a vertex deviation should appear in the correlation of transversal proper motion μ_l and the radial velocity Vr. Although this correlation will be affected by line of sight projection and bulge shape, a significant correlation should be a robust bar indicator. We therefore computed the dispersion tensor σ^2_{ij}. Eigenvalues and eigenvectors of the dispersion tensor correspond to the axis ratio and direction of the axis of the ellipsoid, while the center is given by the velocity first moments. These calculations have been summarized in Table 2.4 and plotted in Figure 2.13. Values σ_r, σ_l and σ_b are the eigenvalues of the velocity ellipsoid and r_S is the Spearman correlation coefficient. Errors on these calculations have been estimated using Bootstrap Montecarlo

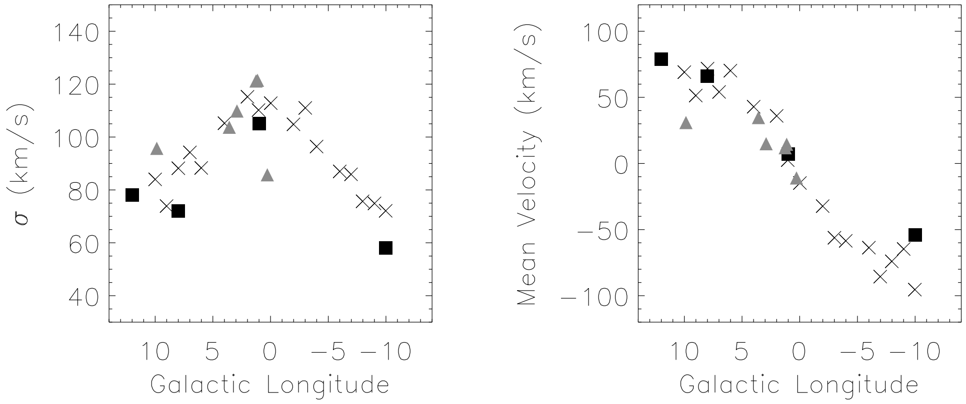

Figure 2.11: Velocity Dispersion σ and Mean Velocity from K-giants by (Minniti 1996) (squares), M-giants by (Rich et al. 2007) (crosses), and our fields (triangles) as a function of the galactic longitude.

Table 2.4: Velocity ellipsoids for galactic minor-axis fields

Field	σ_r km s^{-1}	σ_l km s^{-1}	σ_b km s^{-1}	r_S	Prob(r_S) [a]	l_v [b] deg	N [c]	N_{rej} [d]	N_{iter} [e]
Sgr-I	143±3	135±3	109±3	-0.182	2e-5	-39±6	560	9	3
BW	142±3	118±3	104±5	-0.285	5e-13	-43±4	618	11	4
NGC 6558	79±4	110±4	109±5	-0.108	0.094	-17±7	242	12	4
Sgr-I (turn-off)	154±4	142±4	113±4	-0.170	6e-4	-34±7	397	8	4
Sgr-I (RGB)	112±6	117±6	99±5	-0.200	0.010	-42±9	163	2	1
Sgr-I (blue-MS)	200±8	124±9	172±9	-0.036	0.740	-7±8	86	5	5
BW(turn-off)	146±3	119±3	105±5	-0.292	1e-11	-41±6	514	9	3
BW(RGB)	114±7	114±7	101±6	-0.242	0.013	-40±14	104	1	2
BW(blue-MS)	108±8	132±10	90±9	-0.155	0.190	-21±7	73	1	2

[a] Prob(r_S) corresponds to the significance of the correlation r_S

[b] Vertex angle

[c] Total number of stars selected

[d] Number of rejected stars during clipping procedure

[e] Number of iterations during clipping algorithm

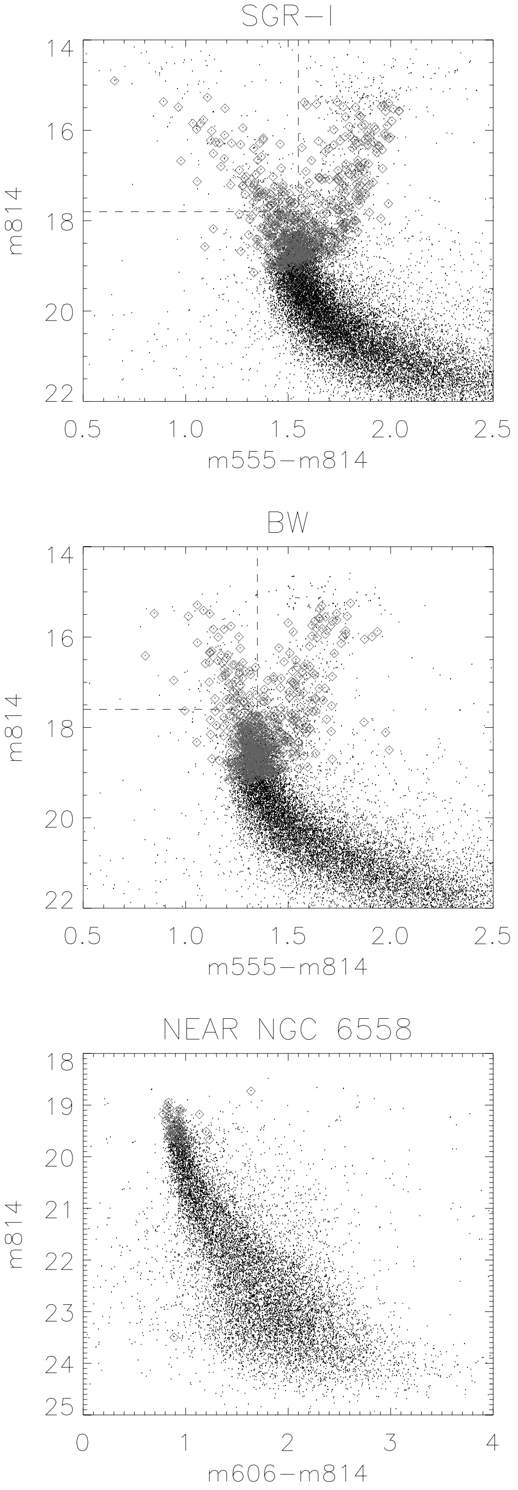

Figure 2.12: CMD for the three minor-axis fields. IFU detections (open squares) have been highlighted over HST detections in each field. Dotted lines in the blue end of the main sequence for Sagittarius-I and Baade's Window fields mark the region in the CMD excluded from bulge analysis due to its proper motions; these are consistent with a foreground population in front of the bulge.

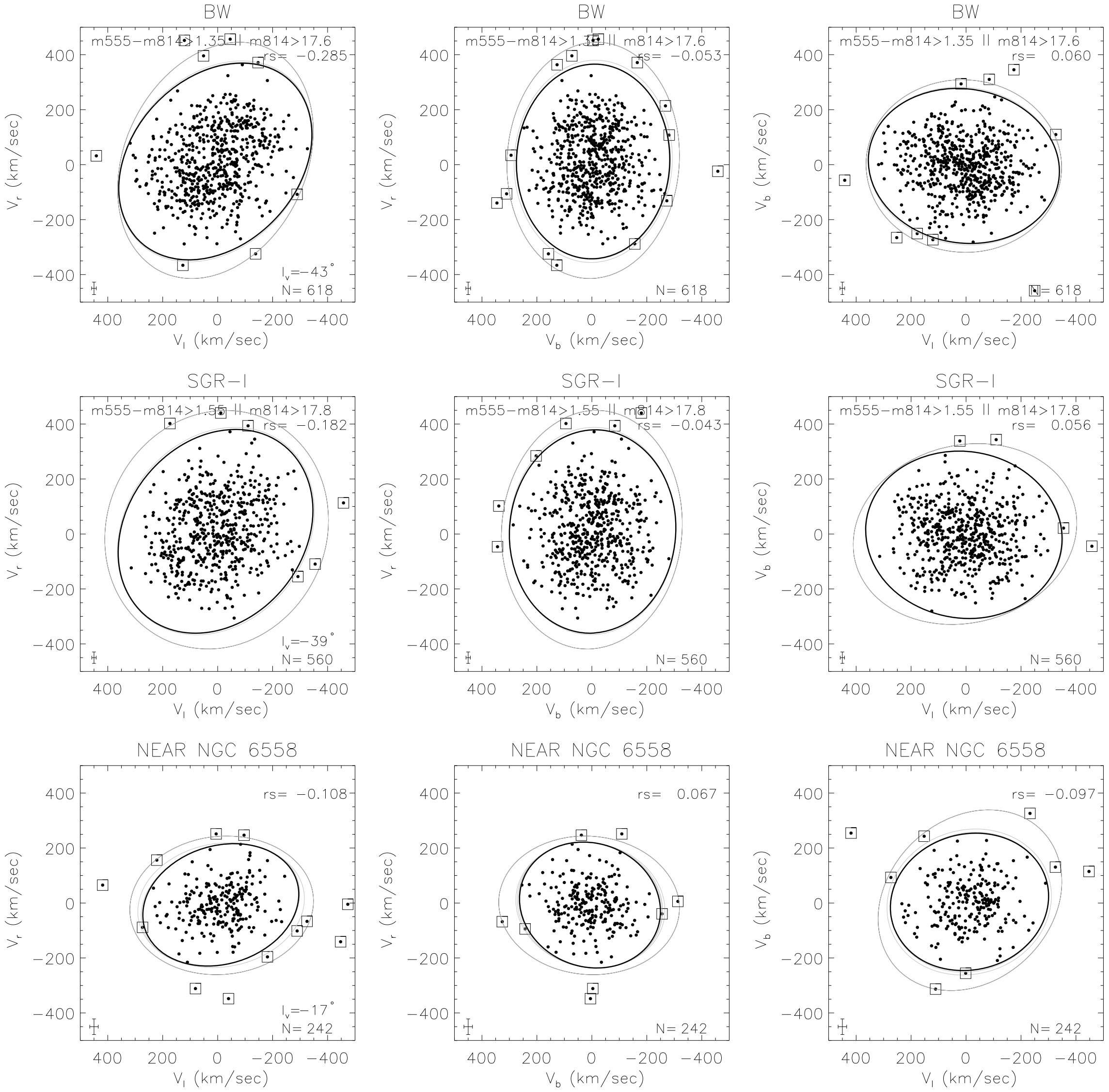

Figure 2.13: Velocity ellipsoids for our minor-axis fields. Correlation between V_l and V_r can be related with bulge triaxility. The color-magnitude selection has been the same shown in Figure 2.12 and numbers of the cuts are shown in every plot when present (e.g. for Sagittarius-I the selection is [m555-m814>1.55 or m814>17.8], which includes turn-off and RGB stars). An iterative clipping algorithm to reject stars outside 3.0 σ of the velocity ellipsoid was used to rid the sample of stars with a kinematic behavior different than the majority. Each figure includes all the velocity ellipsoids to illustrate the convergence of the method. Enclosed points are those rejected for the final velocity ellipsoid for which the parameters found have been included in Table 2.4 . A significant correlation has been found in our three minor-axis fields, Baade's window, Sagittarius-I and NEAR NGC 6558.

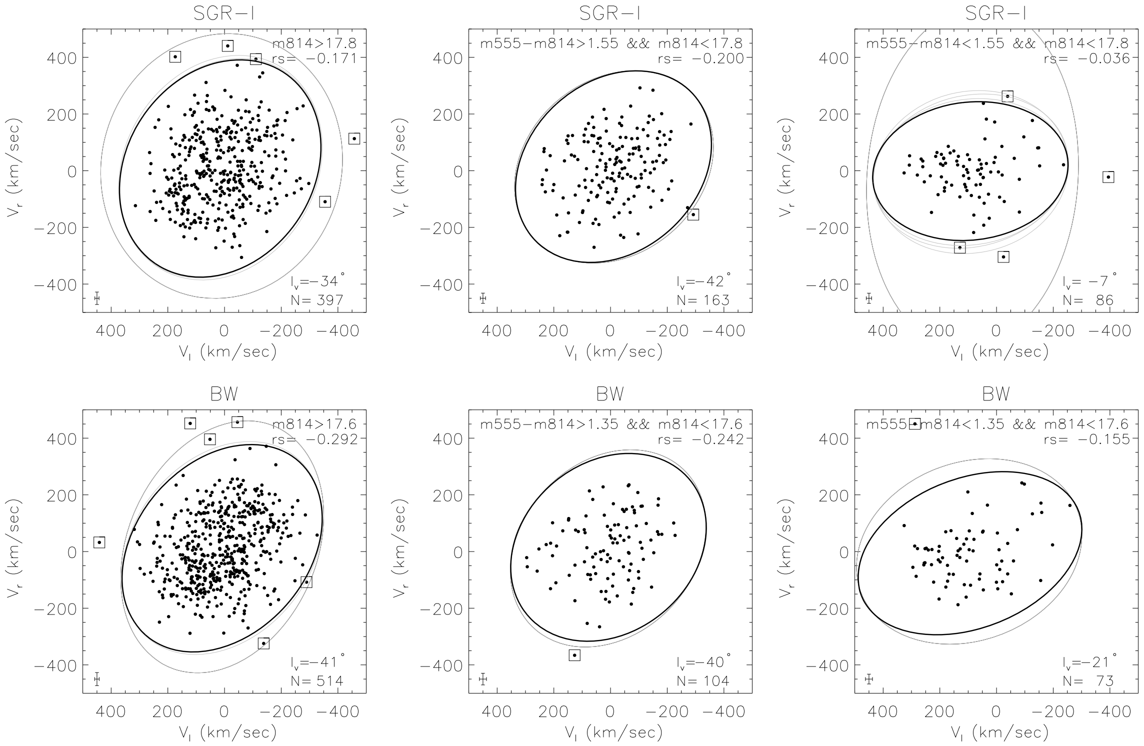

Figure 2.14: Baade's Window and Sagittarius-I velocity ellipsoids for radial velocities (V_r) and transversal proper motion (V_l), divided by population. The region selected is indicated in each plot, and correspond (from left to right) to turn-off, RGB and blue-end of the main sequence.

simulations with 100000 iterations.

The stars shown in Figure 2.13 were selected in the CMD with the same cuts as before. An iterative clipping algorithm was used to derive robust dispersions. Figure 2.13 includes all the iterative velocity ellipsoids, and points within squares are the stars rejected during the process. The values in Table 2.4 are those found in the last velocity ellipsoid. We find a strong correlation in our three minor-axis fields; the vertex deviations are virtually the same for the BW and SGR-I, -43° and -39° respectively, and -17° in NEAR NGC 6558. Similarly the Spearman correlation coefficient r_S shows significant correlation in the three fields, the significance (Prob(r_S)) shows a probability over 99.9% that correlations are real in SGR-I and BW. The latter probability decreases to 91% in the case of NEAR NGC 6558 in agreement with the vertex angle results. Thus, we have a clear trend of an increasing vertex deviation towards the galactic plane in the minor-axis.

Our results agree with previous studies of giants in Baade's window. Even though our selection lacked metallicities, which have been mentioned as a relevant parameter to separate between disk and bulge populations (Minniti 1993, Zhao et al. 1994), the agreement with such samples with well establish metallicities would support our selection criterion. Zhao et al. (1994) analyzed a subsample of 62 stars with metallicities, radial velocities (Rich 1988, 1990) and proper motions from the original sample of 400 K and M giants by Spaenhauer et al. (1992). In the case of Zhao et al (1994), only a vertex deviation was found in the metal rich population of his small sample (39 stars). More recently, the original proper motions by Spaenhauer et al. have been complemented with radial velocity and metallicity measurements (Terndrup et al. 1995, Sadler et al. 1996) allowing us to have ∼300 stars with well defined 3-D kinematics and abundances. The result of this increased sample has been consistent with the preliminary Zhao results (Soto et al. 2007) showing a significant vertex deviation only for the metal rich stars. Moreover, the sample of K giants shows a remarkable agreement in l_v with our own sample of turn-off and main sequence stars, where the angles found are -34° and -41° respectively.

On the other hand, our ellipsoids sometimes show larger dispersion than those found in Zhao, Spergel, & Rich (1994). It can be argued that this increase in dispersion might be caused by contamination by halo or disk stars. By contrast to the Zhao, Spergel, & Rich (1994) small subsample, seleted by abundances, our selection criterion is far more general (only based on the CMD and proper motion information). The Halo population has been found to be ubiquitous through inner fields of the Milky Way, as it has been observed in BW and M22 fields before (Spaenhauer at al. 1992, Minniti et al. 1996). The signatures of a slowly-rotating component would tend to enlarge the dispersion observed. Thus, a contamination by non-bulge stars seems to be reasonable in our sample which has primarily avoided disk contamination using CMD cuts. Furthermore, contamination by Halo stars should be expected to increase in other fields where bulge does not dominate.

As an additional exercise, we have explored the velocity ellipsoids for Sagittarius-I and BW, dividing the sample in turn-off, blue-end of the main sequence and red giant branch. In order to separate those populations, we have used the same limits in color and magnitudes as before to exclude disk stars. Table 2.4 and Figure 2.14 show these ellipsoids. Turn-off selection from the color-magnitude cuts concentrate most of the stars in both samples, repeating the distribution observed in Figure 2.13. Similarly, RGB velocity ellipsoids follow the same trend as expected by KR02 binned CMD. At the same time, bright blue main sequence stars show no significant correlation in both fields, where the velocity ellipsoids have converged to vertex angles of ∼10° as would be expected by a foreground population in front of the bulge. All this evidence suggest that our method has successfully isolated the bulge population kinematically, avoiding foreground disk contamination and highlighting bar features. Furthermore, the fact that the vertex angle decreases at higher latitudes gives us some clues about the extent of the dynamical influence of the bar feature in the galactic bulge. We are in the process of incorporating this information into a detailed dynamical model of the bulge/bar.

2.5 CONCLUSIONS

We have described in this paper the procedures and results of a study which aims to identify a significant signature of the stellar bar in several windows with low foreground extinction in the galactic bulge. Radial velocities have been derived from ~ 110 hours of VLT VIMOS-IFU observations.

We have proven that our new methods which combines the information from HST photometry, proper motions, and IFU spectroscopy makes feasible the detection of the 3-D kinematics of bulge stars. The radial velocity procedure, based on a deconvolution in the spectral IFU cube using HST positions and a IFU PSF have allowed us to obtain more than ∼3200 stellar radial velocities.

Our large amount of data, combined with the proper motion information already presented in KR02 and K04, have allowed the detection of a significant vertex deviation in our three minor-axis fields, Sagittarius-I, BW and NEAR NGC 6558. The fact that the bar presents its strongest signature in the first two fields decreasing in the lower latitude field NEAR NGC 6558, delivers valuable information about the extent of the bar feature and must be intrinsically related to the detailed structure of the galactic bulge.

This project is still in progress, to the six fields with radial velocities and the proper motion in the three central fields, we will soon add proper motion for our three off-axis fields. Four additional fields with radial velocities and proper motion at negative longitudes have been planned. Thus, our project will sample both ends of the bar obtaining robust constraints in the characteristic bulge parameters. Moreover, a self consistent Schwarzschild model to disentangle the kinematic information in these ten fields is under development. In the end, we expect to determine a detailed picture of the stellar bar and its parameters using the radial velocities and proper motions in our fields.

REFERENCES

Anderson, J., & King, I.R. 1999, PASP, 111, 1095

Anderson, J., & King, I.R. 2000, PASP, 112, 1360

Athanassoula, E. 2005, MNRAS, 358, 1477

Benjamin, R.A., et al. 2005, ApJ, 630, L149

Binney, J., Gerhard, O.E., Stark, A.A., Bally, J., Uchida, K.I. 1991, MNRAS, 252, 210

Cudworth, K.M. 1986, AJ, 92, 348

Dwek, E., et al. 1995, ApJ 445, 716

Englmaier, P., and Gerhard, O. 1999, MNRAS, 304, 512

Holtzman, J.A., Watson, A.M., Baum, W.A., Gillmair, C.J., Groth, E.J, Light, R.M., Lynds, R., & O'Neill, E.J., Jr. 1998, AJ, 115, 1946

Kuijken, K., Merrifield, M.R., ApJ, 443, L13

Kuijken, K., & Rich, R.M. 2002, AJ, 124, 2054 (KR02)

Kuijken, K. 2004, ASPC 317: *Milky Way Surveys: The Structure and Evolution of our Galaxy*, Eds. D. Clemens, R. Shah, and T. Brainerd, 310 (K04)

Minniti, D. 1993, IAUS 153: *Galactic bulges*, Eds. Herwig DeJonghe and Harm Jan Habing, 315

Minniti, D. 1996, ApJ, 459, 175

Rich, R.M. 1988, AJ, 95, 828

Rich, R.M. 1990, ApJ, 362, 604

Rich, R.M., Reitzel, D.B., Howard, C.D., Zhao, H. 2007, ApJ, 658, L29

McWilliam, A., Rich, R.M. 1994, ApJS, 91, 749

Sadler, E.M., Rich, R.M., Terndrup, D.M. 1996, AJ, 112 171

Spaenhauer, A., Jones, B.F., Withford, E. 1992, AJ, 103, 297

Schwarzschild, M. 1979, ApJ, 232, 236

Schwarzschild, M. 1982, ApJ, 263, 599

Soto, M., Rich, R.M., Kuijken, K. 2007, ApJ, 665, L31

Terndrup, D.M., Rich, R.M., Sadler, E.M., 1995, AJ, 110, 1774

Tonry, J., & Davis, M. 1979, AJ, 84, 10

Zeballos, H., Soto, M., Kuijken, K, Rich, R.M. 2008, (in preparation)

Zhao, H.S., Spergel, D.N., Rich, R.M. 1994, AJ, 108, 2154

Zhao, H.S., Rich, R.M., & Spergel, D.N. 1996, MNRAS, 282, 175

Zhao, H.S. 1996, MNRAS, 283, 149

Zoccali, M., et al. 2006, A&A, 457, L1